Lasers in Manufacturing Conference 2023

Investigation on the correlations between heat accumulations and actual part defects during laser powder bed fusion using heat maps

Sven Müller[a,*], Ronald Pordzik[a], Thorsten Mattulat[a]

[a]*BIAS – Bremer Institut für angewandte Strahltechnik GmbH, Klagenfurter Straße 5, 28359 Bremen,Germany*

Abstract

During laser powder bed fusion processes, heat accumulations can lead to e.g. annealing colors, increased porosity or protruding edges and are one of the reasons for the necessity of support structures. Using constant manufacturing process parameters, heat accumulations often cannot be avoided due to varying heat dissipation cross sections and gradients. In order to selectively avoid heat accumulations, it is necessary to identify in which part sections heat accumulations occur and at what extent heat accumulations become critical for the part quality. In this study, coaxial two-channel pyrometric measurements are used to generate high-resolution heat maps of the individual layers during laser powder bed fusion. Suitable methods for benchmarking heat accumulations with inner and outer part quality (e. g. porosity) are presented for different geometry characteristics like varying overhang angles, part volumes and shapes. The suitability of such heat maps to identify and visualize especially heat accumulations critical for part quality is analyzed.

Keywords: Additive Manufacturing; Laser Powder Bed Fusion; Heat Map; Temperature Measurement; Defect Detection

1. Introduction

A significant advantage of laser powder bed fusion (LPBF) is the high degree of design freedom with near net shape production, which means that complex components - including geometries that cannot be realized in any other way - can be produced economically even in small quantities. However, heat accumulations during the LPBF process can lead to inadequate geometric and mechanical properties or even result in

* Corresponding author. Tel.: +49-421-218-58077; fax: +49-421-218-58063.
E-mail address: mueller@bias.de.

process failure. The primary reason for the high relevance of heat accumulations in the LPBF process is the low thermal conductivity within the powder bed and thus the low heat dissipation into and across the powder bed. In this regard, Rombouts et al. have shown that the thermal conductivity of a steel (316L) powder bed is in the range of one percent of the thermal conductivity of the solid material for different powder particle sizes from 22 µm to 85 µm and relative powder densities from 54% to 60% (Rombouts et al., 2005). Since the powder bed can only dissipate a small part of the introduced heat from the process zone, the main heat dissipation takes place via the already manufactured structures.

One approach for identifying and quantifying heat accumulations is the measurement of the maximum temperature occurring during the process. Hence, the measurement of temperature and thermal radiation during LPBF via pyrometric methods is a widely studied topic. Both single- and two-channel pyrometry have already been applied. The single channel measurement has the disadvantage that the knowledge of the material and surface dependent emissivity is necessary to calculate the absolute temperature from the radiation intensity (Moylan et al., 2014). This measurement approach is used e. g. by Mohr et al. to study heat accumulations during a LPBF process with a gradually reduced cross-sectional area for heat dissipation (Mohr et al., 2020-1). They simplify the measurement method by not calibrating the emissivity, which allows for a qualitative insight regarding the heat accumulations in the manufacturing process, while absolute temperatures cannot be determined. Two-channel pyrometry records two wavelength ranges, making the measurement virtually independent of emissivity. This approach has also been applied to the LPBF process by Pavlov et al. by integrating a two-channel pyrometer coaxially into the beam path of the laser (Pavlov et al., 2010). However, the absolute temperature in this case is not given either since the coaxial integration would require a calibration of the measuring device in the beam path. A coaxially integrated two-channel approach calibrated to the beam path is presented by Tyralla and Seefeld, whereby measurement shifts due to different absorption behaviors of the optics in the beam path with respect to the two spectral ranges of channel 1 and channel 2 of the pyrometer are eliminated. (Tyralla et al., 2019).

A distinction between point- and imaging-based temperature measurement should also be mentioned. The LPBF process was observed e. g. by Bayle et al. using a point pyrometer to determine the temperature change before, during and after the laser process at specific locations within the component layer (Bayle et al., 2008). Thermography also plays a role when it comes to the LPBF process, since it allows to visualize heat accumulations (Mohr et al., 2020-2) and to evaluate geometrical parameters such as the melt pool size (Tyralla et al., 2020) or the heat distribution during the buildup process (Craeghs et al., 2011). Using uncalibrated single-channel thermographic images of the powder bed, Ulbricht et al. were able to determine cooling rates after each component layer and visualize them spatially resolved (Ulbricht et al., 2020).

While different methodologies for measuring temperature during LPBF processes are already widely used, the correlation between heat accumulations and actual part defects is not sufficiently analyzed. Using heat maps, based on position and time correlated, high speed coaxial two-channel pyrometric measurements, first results regarding said correlation are given in this work.

2. Experimental

In this study, 1.4404 (316L) powder with a particle size distribution between the limits of 15 µm and 45 µm and 1.4301 substrates were used for LPBF. The utilized LPBF setup consists of laser scan head (fiberSYS from SCANLAB), a 2 kW fiber laser (TruFiber 2000 P compact from Trumpf) and a process chamber with a build plate diameter of 80 mm. The used fiber laser has a minimum and maximum effective laser power of 30 W and 2000 W respectively. The beam diameter in the working plane is 55 µm with a gaussian-like beam distribution. Argon (purity 4.8) was used to create an inert gas atmosphere with an oxygen level smaller than 0.1%. For all samples, a bi-directional scanning strategy with varying rotations (51° or 90°) of the

scanning vectors between the individual layers was utilized. The volume energy density was adopted by varying the laser power and scanning speed while the layer thickness and hatching distance were kept constant at 20 µm and 80 µm respectively. For coaxial temperature measurements during the LPBF process, a high-speed two-channel pyrometer (H322 from Sensortherm), calibrated to the beam path, was used with a measurement frequency of 25 kHz, a spectral range 1.65 µm to 1.8 µm and 1.45 µm to 1.65 µm for channel 1 and channel 2 respectively as well as a measurement range from 700 °C to 2300 °C (see Figure 1). Since the beam path calibration was only done at a reference temperature of 1200 °C, the measurements are not given as absolute temperatures in this work. The standard response time t_{90}, which indicates the time it takes for the pyrometer to display 90% of a sudden temperature change (increase) of an object at the signal output, is 1 ms and can be adjusted to a minimum of 0.08 ms. Due to the high scanning speeds during LPBF, a pyrometer response time t_{90} of 1 ms leads to limited measurement detail quality. Based on this it is to be expected that locally limited temperature variations cannot be resolved. However, since a relevant portion of industrially available pyrometers are limited to a minimum response time of 1 ms it is of relevance to also analyze the potential of such measurements.

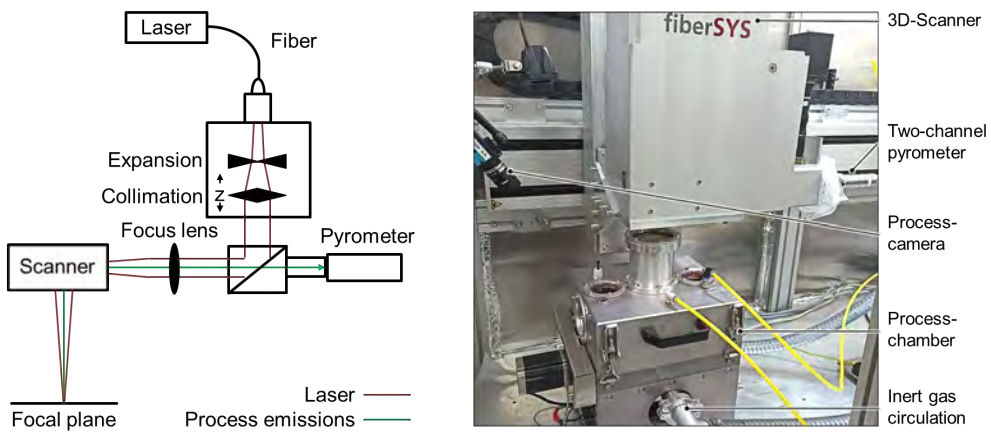

Fig. 1. LPBF setup with coaxial two-channel pyrometer.

To compensate for tracking errors of the scanner, a ScanFieldMonitor (from Primes) was used to determine the relevant delay times (e. g. laser on delay). During the LPBF process, the coordinates of the scanner and the sensor signal of the two-channel pyrometer are synchronized using a real-time interface (Open Interface Extension from SCANLAB). In case of the measurements with a response time of 1 ms, all coordinates of the scanner path (including jumps between vectors) and sensor signals are recorded, while measurements with a sensor signal below 1400 are not considered for the generation of the heat maps. While this is a simple method to subdivide measurements that allegedly lie in- and outside of actual melt pools, it cannot be assured that no relevant measurement points are neglected. In case of measurements with a response time of 0.08 ms, the setup was optimized so that only coordinates and sensor signals are recorded while the laser is turned on. This assures that all relevant measurement points are considered. However, some measurement points are already recorded during the time frame between the laser being turned on and an actual melt pool being formed. At the current state of the setup, it is not compensated for this behavior so that the resulting comparatively cold measurement points at the beginning of the scanned vectors are included during heat map generation. In both cases, a measurement field is generated in which the recorded temperatures are plotted at their corresponding measurement locations for each layer. Further a pixel-grid

with variable pixel sizes is then superimposed on this field. The average temperature of all measured temperatures covered by a pixel is calculated and stored accordingly, resulting in a heat map (see Figure 2).

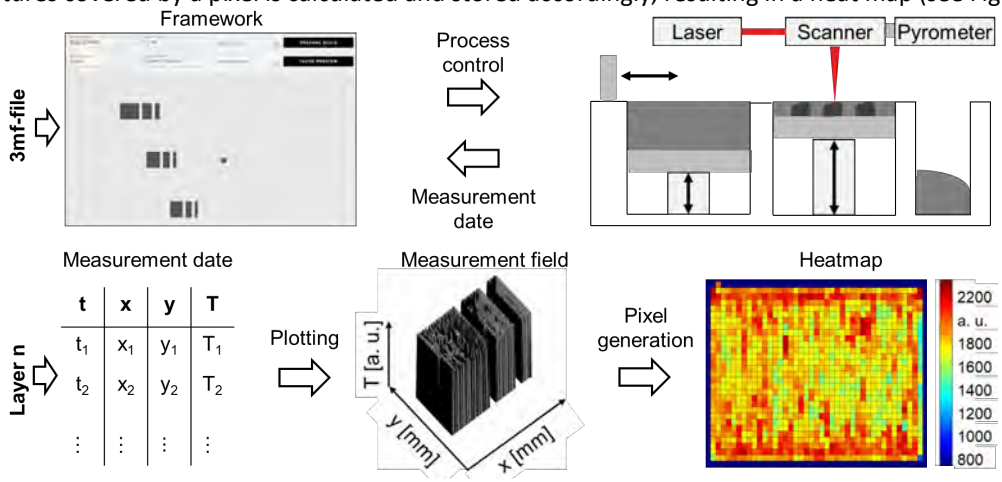

Fig. 2. Generation of heat maps based on position correlated coaxial pyrometric temperature measurements.

The part porosities were determined using vertical cross-sections and a contrast-based image analysis. For this, a light microscope (ZEISS Axio) and the 'Olympus Stream' analysis software were utilized.

3. Results

To investigate the influence of different volume energy densities and porosities on the temperature field of the heat maps, energy densities resulting in lack-of-fusion pores, virtually no pores and gas/ keyhole pores were used. Thereby the response time of the pyrometer was kept constant at 1 ms. A clear distinction between the three different cases can be seen in the temperature field of the heat maps (see Figure 3). When lack-of-fusion pores are present, a relatively cold and uneven temperature field can be seen. In case of virtually no pores being present, a comparatively even and higher temperature field is found. Once gas/ keyhole pores are present, an even higher temperature field, limited by the measurement range of the pyrometer, with local irregularities can be seen. On the right-hand side of the heat map of all parts, one colder pixel row can be seen. This pixel row correlates with the first incoming, in y-direction oriented scanning vector of each layer.

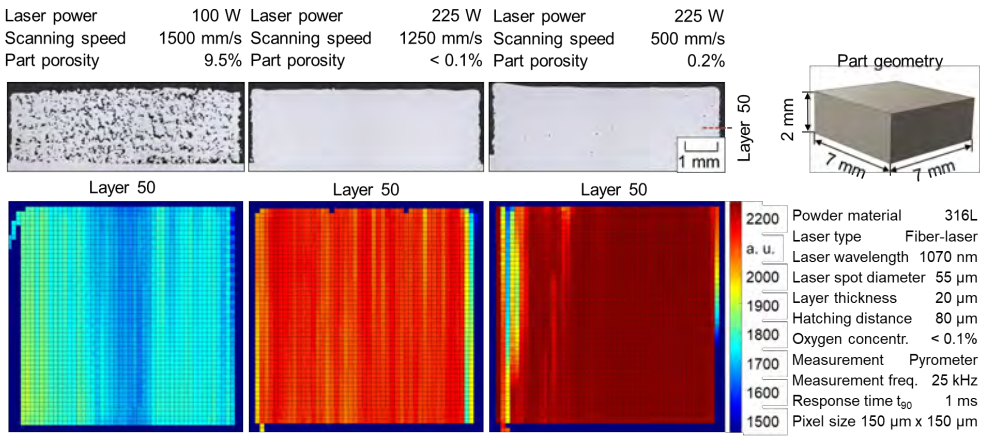

Fig. 3. Correlation between lack-of-fusion pores, virtually no pores, gas/ keyhole pores and heat map temperature fields.

In Figure 4 the average part temperature, calculated using the measurements of all layers of each part, with the corresponding standard deviation can be seen for different volume energy densities. In accordance with the results of the heat map temperature fields in Figure 3, the average part temperature increases with increasing volume energy densities. However, at the highest volume energy densities no further temperature increase can be seen due to the limited measurement range of the pyrometer.

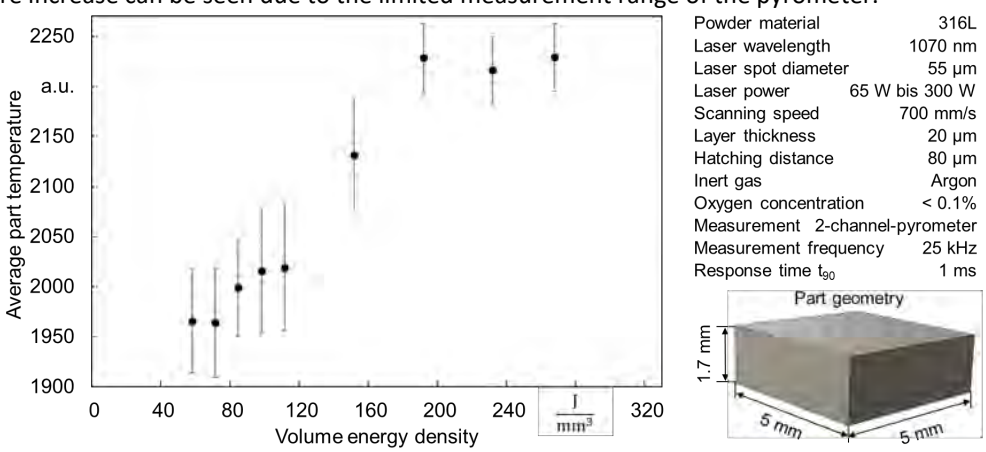

Fig. 4. Influence of varying volume energy densities on the average part temperatures.

In Figure 5 the average part temperature is plotted over the party porosity. In correlation with Figure 3, the part porosity increases with decreasing average part temperature in the analyzed energy density range. It can also be seen that the standard deviation of the average part temperature is significantly lower for parts with porosities smaller than 0.3% compared to parts with higher porosities.

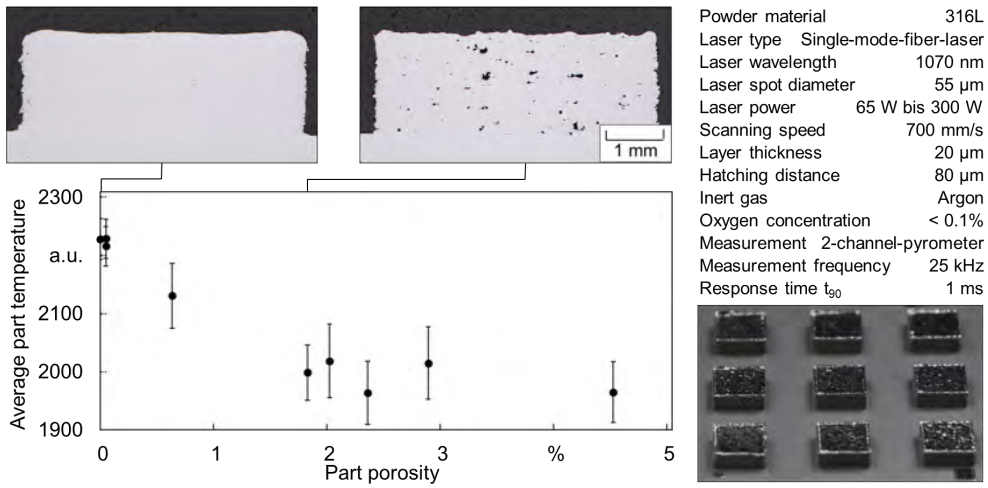

Fig. 5. Correlation between part porosity and average part temperature as well as standard deviation of the average part temperature.

To analyze the influence of different pyrometer response times on the heat map detail quality, the standard response time of 1 ms was compared to a response time of 0.08 ms using identical process parameters for both configurations and a bead-on-plate approach (see Figure 6).

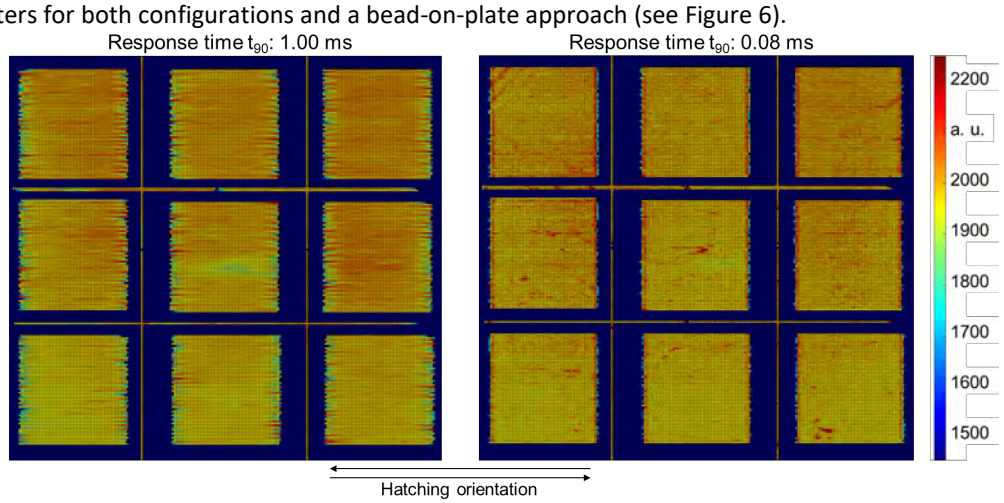

Fig. 6. Influence of different pyrometer response times t_{90} on the heat map detail quality for identical process parameters.

As can be seen in Figure 6, the detail quality of the heat maps increases strongly when reducing the response time. Using the smaller response time, additional details can be seen in the center of the bead-on-plate samples depicted in Figure 6, while the heat map becomes much clearer especially towards the part edges. Thereby, higher temperatures can locally be found in the edges along the hatching orientation.

Using a pyrometer response time of 0.08 ms during the manufacturing of overhanging walls with an overhang angle of 25°, in accordance with Figure 6, additional details can be seen in the resulting heat maps (see Figure 7). Heat accumulations at the edges of the layers become visible, while protruding edges can be seen in the cross section image.

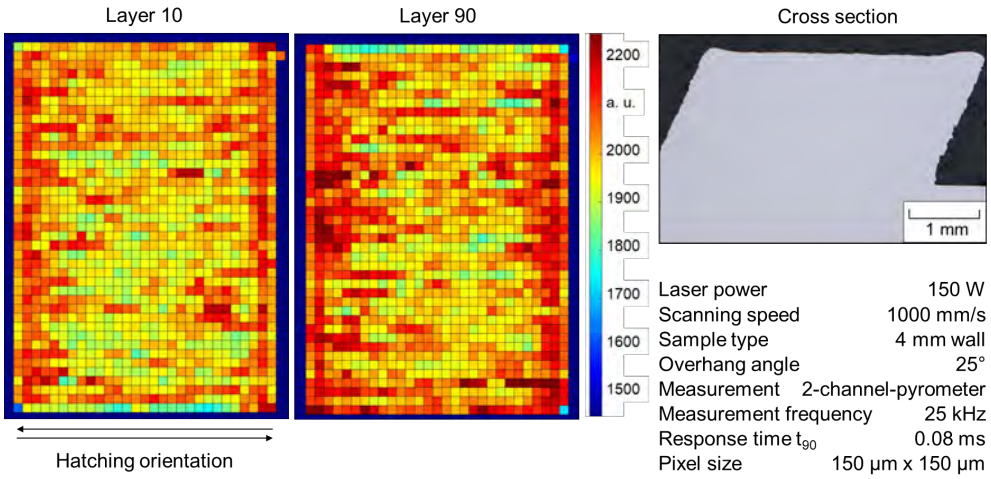

Fig. 7. Heat maps of an overhanging wall sample (25°) with high detail quality (pyrometer response time of 0.08 ms).

Figure 8 shows the heat maps of layer 10 and layer 90 of wall samples with thicknesses of 1.0 mm, 2.0 mm and 3.0 mm. It can be seen that the smaller wall thicknesses result in heat accumulations. However, the part quality (porosity, surface quality) does not significantly vary between the different wall thicknesses.

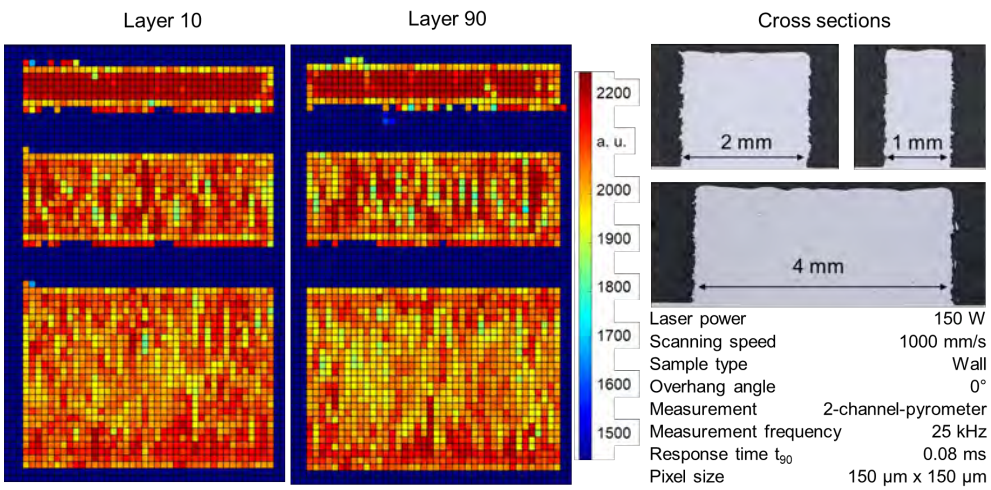

Fig. 8. Heat maps of wall samples with high detail quality (pyrometer response time of 0.08 ms) and varying wall thicknesses.

Figure 9 shows the heat maps of layer 10 and layer 90 of overhanging wall samples (50°) with thicknesses of 1.5 mm, 3.0 mm and 6.0 mm. In accordance with Figure 8, the smallest wall thickness results in a visible heat accumulation, reaching the measurement limit of the used pyrometer. This can also be seen in the cross sections, where first individual gas/ keyhole pores can be seen for the 1.5 mm wall sample. At the same time the surface quality (mainly overhanging and top surface) of the 1.5 mm wall sample decreases slightly compared to the other two samples. Similar to Figure 7, a slight heat accumulation can be seen at the edges of the overhanging wall samples with a thickness of 3.0 mm and 6.0 mm.

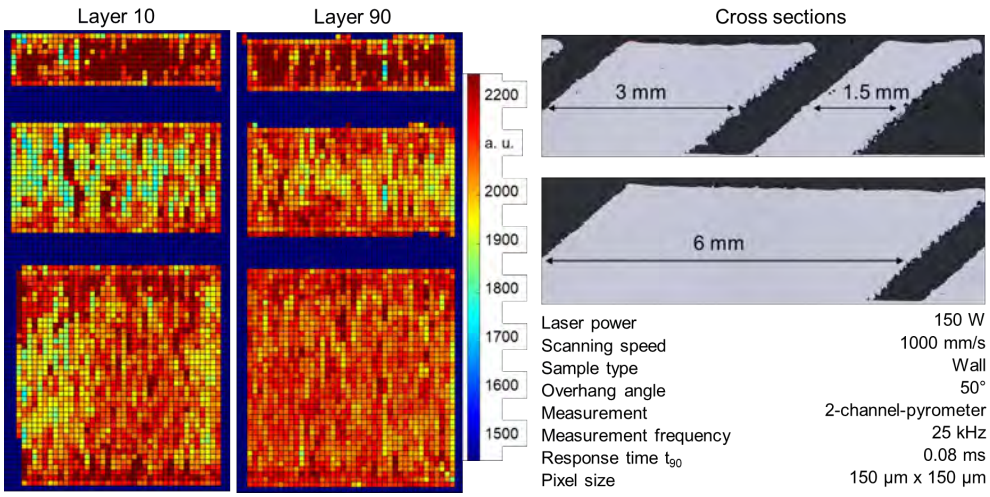

Fig. 9. Heat maps of overhanging wall samples (50°) with high detail quality (pyrometer response time of 0.08 ms) and varying wall thicknesses.

4. Discussion

Based on heat maps acquired with a response time of 1 ms, samples with lack-of-fusion pores show a relatively cold and uneven temperature field (see Figure 3). Since the induced energy in this case is not sufficient to fully melt all powder particles, this is to be expected. The high standard deviation of the average part temperature of such samples with comparatively high porosity (see Figure 5) can be deduced to limited process uniformity / stability. Samples with virtually no pores show a comparatively even and hotter temperature field (see Figure 3) as well as small standard deviations of the average part temperature (see Figure 5), correlating with a uniform process behavior. Once gas / keyhole pores are present the heat map temperature field reaches the limit of the pyrometer measurement range, while still a clear differentiation to the heat maps of samples with virtually no pores can be seen. Occurring partial temperature deviations in heat maps of sample with gas/ keyhole pores indicate a reduction of the process stability. Transferring these heat maps results into average part temperatures (see Figure 5), a quantitative correlation between part porosity and heat map temperature field can be determined. For the inner volume of LPBF samples hence an ideal temperature range exists which leads to virtually no pores while temperatures below or above result in lack-of-fusion pores or gas/ keyhole pores respectively. This ideal temperature range is dependent on the used powder material as well as the pyrometric setup (e. g. calibration to the beam path), while it is to be expected that further process parameters like layer thickness also influence this ideal temperature range. While the porosity of the inner volume of the samples can be correlated with heat maps generated with a response time of 1 ms, local heat accumulations, especially at the part edges (transition between hot / melt pool and cold / powder bed and vice versa), cannot be resolved (compare Figure 3). This originates in the fading phenomena occurring based on the high pyrometer response time.

Reducing the pyrometer response time t_{90} to 0.08 ms, as to be expected, the detail quality of the heat maps increases (see Figure 6). Local irregular temperature variations can be seen mainly in the inner section of such high detail heat maps (compare Figure 7). Based on the extend of these irregularities, it is to be expected that besides possible actual melt pool temperature variations also measurement irregularities are responsible for this behavior. Such measurement irregularities could originate from varying emissivity ratios due to varying melt pool characteristics like surface structure / angle and oxide layers. Based on this the

measured two-channel temperature could vary strongly while the actual melt pool temperatures may only differ slightly. Since two-channel pyrometric measurements are most dominantly influenced by the hottest temperature inside of the measurement field, also a varying keyhole stability could possibly influence the measurement. However, beside the measured temperature variations, heat accumulations towards the part edges can be seen and correlated with protruding edges (see Figure 7). This phenomenon is mainly present along the hatching direction. Considering the bi-directional hatching strategy, this heat accumulation could be based on the higher energy amount introduced into the edge in a given time, based on the reversal of the scanning direction. It is to be noted, that the actual reversal point of course lies outside of the part limits to avoid acceleration and deceleration influences. The heat accumulation at the part edges increases slightly in build direction which can be explained by increasing influences of the overhang angle as well as the increasing distance from the substrate which limits heat dissipation. In Figure 8 a similar phenomenon can be seen for decreasing wall thicknesses, where the smallest wall thickness results in the highest heat map temperature field. As expected in comparison with Figure 3, for the present temperature field no relevant influence on the part quality (porosity) can be seen in the cross section. While the edges of the heat maps of the wall samples with thickness 2 mm and 4 mm in Figure 8 also show slight heat accumulations, no quantitative correlation can be derived with the height of the protruding edges. Introducing an overhang angle of 50° for samples with different wall thicknesses (see Figure 9), a similar behavior compared to the wall samples with no overhang can be seen. The sample with the smallest wall thickness shows the highest heat accumulation. Based on the extend of the heat accumulation and in correlation with the results in Figure 3, first gas / keyhole pores can be seen. Also, a decrease in surface quality (overhang surface) can be correlated. For the bigger wall thicknesses, similar to Figure 8, slight heat accumulations can be seen at the part edges, while no direct quantitative correlation with the height of the present protruding edges can be derived. This missing quantitative correlation could be based on the influence of measurement irregularities in the two-channel temperature due to varying emissivity ratios and keyhole stabilities as described above.

5. Summary

For heat maps based on position and time correlated coaxial two-channel pyrometric measurements during LPBF and a measurement frequency of 25 kHz it could be shown that,

- a quantitative correlation between part porosity and heat map/ part temperature can be found, whereby an ideal temperature range exists which leads to virtually no pores while temperatures below or above result in lack-of-fusion pores or gas/ keyhole pores respectively;
- using a standard pyrometer response time t_{90} of 1 ms the detail quality of the heat maps is not sufficient to visualize local heat accumulations especially towards part edges and correlate them with actual local part defects like protruding edges;
- using a pyrometer response time t_{90} of 0.08 ms increases the detail quality of the heat maps sufficiently to qualitatively correlate heat accumulations at part edges with protruding edges. However, no reliable quantitative correlation between heat accumulations at the part edges and the height of the protruding edges could be found with the current heat map accuracy and corresponding detail quality.

Acknowledgements

The IGF-Project with the IGF-No.: 22.039 N / DVS-No.: 13.3470 of the “Forschungsvereinigung Schweißen und verwandte Verfahren e. V.” of the German Welding Society (DVS), Aachener Str. 172, 40223 Düsseldorf was funded by the Federal Ministry for Economic Affairs and Climate Action (BMWK) via the German Federation of Industrial Research Associations (AiF) in accordance with the policy to support the Industrial Collective Research (IGF) on the basis of a decision by the German Bundestag. Furthermore, the authors gratefully acknowledge the collaboration with the members of the project affiliated committee regarding the support of knowledge, material and equipment over the course of the research.

References

Bayle, F., Doubenskaia, M., 2008. Selective laser melting process monitoring with high speed infra-red camera and pyrometer, Proc. SPIE Fundamentals of Laser Assisted Micro- and Nanotechnologies 6985.

Craeghs, T., Clijsters, S., Yasa, E., Bechmann, F., Berumen, S., Kruth, J.-P., 2011. Determination of geometrical factors in Layerwise Laser Melting using optical process monitoring, Optics and Lasers in Engineering 49, 1440–1446.

Mohr, G., Scheuschner, N., Hilgenberg, K., 2020-1. In situ heat accumulation by geometrical features obstructing heat flux and by reduced inter layer times in laser powder bed fusion of AISI 316L stainless steel, Procedia CIRP 94, 155–160.

Mohr, G., Altenburg, S. J., Ulbricht, A., Heinrich, P., Baum, D., Maierhofer, C., Hilgenberg, K., 2020-2. In-Situ Defect Detection in Laser Powder Bed Fusion by Using Thermography and Optical Tomography—Comparison to Computed Tomography, Metals 10, 103.

Moylan, S., Whitenton, E., Lane, B., Slotwinski, J., 2014. Infrared thermography for laser-based powder bed fusion additive manufacturing processes, AIP Conference Proceedings 1581, 1191–1196.

Pavlov, M., Doubenskaia, M., Smurov, I., 2010. Pyrometric analysis of thermal processes in SLM technology, Physics Procedia 5, 523–531.

Rombouts, M., Froyen, L., Gusarov, A. V., Bentefour, E. H., Glorieux, C., 2005. Photopyroelectric measurement of thermal conductivity of metallic powders, Journal of Applied Physics 97.

Tyralla, D., Seefeld, T., 2019. Thermal based process monitoring for laser powder bed fusion (LPBF), Proceedings of Materials Science and Technology of Additive Manufacturing Conference (MSTAM19).

Tyralla, D., Seefeld, T., 2020. Advanced Process Monitoring in Additive Manufacturing. PhotonicsViews 17, 60–63.

Ulbricht, A., Altenburg, S. J., Sprengel, M., Sommer, K., Mohr, G., Fritsch, T. et al., 2020. Separation of the Formation Mechanisms of Residual Stresses in LPBF 316L. Metals 10.